



Structure dependence of gas sensing responsivity on graphene nanoribbons covered TiO₂ nanotubes, nano-bugles array

Bohr-Ran Huang¹, Yu-Jyun Chen¹, and Shang-Chao Hung^{2,3,*} 

¹ Graduate Institute of Electro-Optical Engineering & Department of Electronic Engineering, National Taiwan University of Science and Technology, Taipei 106, Taiwan, ROC

² Fuzhou Polytechnic, Fuzhou University City, Fuzhou 350108, Fujian, China

³ Intelligent Technology Research Centre, Fuzhou 350108, Fujian, China

Received: 13 July 2021

Accepted: 16 January 2022

Published online:

4 February 2022

© The Author(s), under exclusive licence to Springer Science+Business Media, LLC, part of Springer Nature 2022

ABSTRACT

Titration of various amounts of graphene nanoribbons on titanium dioxide nanotubes (Gr/TNTs) and nano-bugles (Gr/TNBs) with different apertures to form composite nanostructures, and using them as gas sensing layers, have been achieved successfully and confirmed by FESEM observation, Raman spectra comparisons, XRD and FTIR measurements. The Gr/TNBs sensors show higher hydrogen gas response than corresponding Gr/TNTs sensors over the 100–2000 ppm range; this suggests that altering sensing morphology can improve gas sensing capability. A composition effect is found on Gr/TNBs sensors, and this effect is more pronounced with higher graphene concentration. On the other hand, heavier graphene content on Gr/TNTs sensors does not seem to affect their sensing capability much. Also, measuring hydrogen gas sensitivity under fixed gas concentration for 40 V Gr/TNB sensors shows a strong linear correlation between graphene concentration and responsivity. Yet measurement on 40 V Gr/TNTs sensors, at relatively low gas concentration of 100 ppm, shows that increase in graphene content hardly affects their responsivity. Gr/TNTs sensors fabricated with both smaller and larger tubular apertures produce this same result, too. Lastly, gas diffusion interactions between two-dimensional layered graphene structure and various geometries of TiO₂ are fully discussed.

1 Introduction

Chemo-resistors [1] are to date more widely used than field-effect transistors (FET) [2, 3], surface acoustic wave sensors [4], and optical fiber sensors

[5]. They meet manufacturing requirements of high sensitivity, high selectivity, low operating temperature, and low-cost for use as portable gas/vapor sensors. Metal oxide family, owing to its superior chemical and thermal constancy, production adaptability and low cost, has received wide attention for

Address correspondence to E-mail: schung99@gmail.com

gas sensor development. Due to gas molecule adsorption and desorption on the surface of metal oxide, the transfer of electrons will vary carrier concentration and results in a change of conductance. However, the characteristic of adsorbing gas molecules on the surface of the membrane is largely dependent on morphologies and dimensions of those structures. Subsequently, nano metal oxides with layered structures and diverse geometries are found to be attractive materials for preparing gas sensing devices such as $\text{TiO}_2/\text{Cu}_2\text{O}/\text{CuO}$ multi-nanolayers [6], capacitor-like $\text{Pt}/\text{TiO}_2/\text{Pt}$ structures [7]. Compared with other one-dimensional nano-structured materials, titanium dioxide (TiO_2) nanotube is considered to be the best candidate for gas sensing applications because of its unique mechanical structure properties. Meanwhile, graphene and graphene-related material, such as two-dimensional (2D) sp^2 -bonded structure nanomaterial, with its flexibility, optimal specific surface area and excellent mechanical strength, is another attractive material. Its unique chemical structure, ultrafast electron mobility and outstanding electrochemical performance result in very extensive application in supercapacitors [8], electrocatalysis [9], surfactant [10], photoelectrocatalysis [11], and organic photovoltaic cells [12]. These exclusive properties over other materials have been utilized in the construction of portable and flexible sensing devices. Recently, a variety of graphene-based sensors for specific uses, such as humidity sensing [13, 14], biosensing [15] non-enzymatic glucose sensing [16–18], bending sensing [19], pressure sensing [20], strain sensing [21, 22] and electrochemical sensing [23, 24], have shown practical applications in many areas including environmental monitoring [25, 26], food science research [27] and human healthcare [28]. In particular, graphene-based gas sensors, which have been predicted via theoretical studies [29, 30], and proven by experimental evaluation [31] that the responsivity can be varied by absorption of gas molecules on the graphene surface. This sensing capability is comparable with the nanoparticles at sensing surface modifications. Considerable effort has been focused on optimizing sensing parameters, preferential doping and decoration of nanoparticles such as Co [32], Cr [33], and Pd [34] on TiO_2 nanostructures to enhance the sensing performance for H_2 detection. Because of the different work functions of the decorating materials and chemical catalysis effects, these modifications can

change the Schottky barrier, and therefore improve the TiO_2 nanotubes sensing properties. On the other hand, the work on the geometries of nanoscale multilayered structures such as $\text{TiO}_2/\text{Cu}_2\text{O}/\text{CuO}$ [6], $\text{Pt}/\text{TiO}_2/\text{Pt}$ [7, 35] have also been realized that lattice matched in heteroepitaxial interfaces [6] or less thickness of the film in capacitor-like structures [7] result in much better performance. Therefore, the study of 2-D material layer covered on 1-D TiO_2 nanotubes as sensing layer could be another attractive issue. In this work, we successfully produce the composite nanostructures as the gas detecting layer; it is made by adhering two-dimensional graphene material to both tubular and bugle-shaped TiO_2 structures via plasma treatment. We also found the structures dependence of gas sensing responsivity and thoroughly discuss the aggravation of composition effect with increased graphene content.

2 Experiment

Crystallized titania nanotubes (TNTs) specimens with different apertures in this study were synthesized from pure Ti foils (99.6% purity, purchased from Nilaco Co. 200 mm \times 100 mm \times 0.1 mm) via electrochemical anodization methods with an ethylene glycol solution containing 0.5 wt% NH_4F (98% purity, purchased from Acros organics Co.) and 2.5 vol% deionized water in applied voltage of 20, 30, 40, 50 V, respectively. Crystallized titania nano-bugles (TNBs) specimens were fabricated from TNTs by immersing in H_2O_2 solution (30%–31%, purchased from Sigma-Aldrich Co.) for 1 h at room temperature. Details of fabrication and crystallization process of tubular and bugle-shape nanostructures of TiO_2 can be found in prior reports [36]. To modify the TiO_2 surfaces, all the TNTs and TNBs specimens fabricating with various applied voltage were cleaned with deionized water and subjected to plasma treatment with power of 1000 W for 30 min. The graphene (Gr) nanoribbon (98% purity, purchased from Elecmat Co.) solution with 5 wt% was then respectively dropped in quantities of 0.3, 0.6, 0.9 ml on the surface of TNTs and TNBs specimens to obtain the Gr/TNTs and Gr/TNBs specimens with three different Gr composition. The as-obtained specimens were rinsed with deionized water and air-dried. Schematic diagrams of the fabrication process of Gr/TNTs and Gr/TNBs are shown in Fig. 1.

The behavior of surface Ti–OH groups, crystallinity, structures, and surface morphologies of the all as prepared specimens were monitored using Raman spectroscopy with an excitation wavelength of 514.5 nm, Fourier transform infrared (FTIR) spectrum recording over the range 600 to 4000 cm^{-1} on spectrometer (Bomem, DA 8.3, CANADA) to investigate the reactivity of binding energy, X-ray diffractometer (XRD, D2PHASER-X-ray Powder Diffraction, Bruker) with $\text{CuK}\alpha 1$ radiation ($\lambda = 1.54056 \text{ \AA}$), and field emission scanning electron microscope (FESEM, JSM-6500F), respectively.

All the sensing specimens were then prepared with finger type electrode geometry of Pt electrodes which were sputtered onto the layer of sensing material with 30 nm thickness. The width of overlapping electrodes and the gap between two successive electrodes was 0.5 mm. The DC sputtering system operating on pressure, current, and the time period were 4.5×10^{-3} bar, 10 mA, and 600 s, respectively. The Gr/TNTs and Gr/TNBs specimens were subsequently placed in a sealed chamber and then measured its resistivity in air to investigate the gas sensing properties. The measurement performed continuously in the presence of gaseous hydrogen and air switching. At the end of the experiment, the resistivity of the sample in air was measured again.

3 Results and discussion

Figures 2 and 3 collectively show the remarkable differences on the surface morphology of Gr/TNTs and Gr/TNBs respectively fabricated with applied voltages of 20 to 50 V decorating with different Gr compositions. TNTs are clearly seen as a high density, perpendicular and side by side structures on the Gr uncovered area as shown in Fig. 2. It is found that as electrochemical anodization applied voltages increase from 20 to 50 V, the average diameters and the average lengths of the TNTs respectively increase from 25 to 100 nm and 1.4 to 4.1 μm . The average diameters ($2r$) of TNTs could be estimated from the top-view FESEM image. The length (L) of TNTs also could be estimated from cross-section morphology of FESEM images in prior report [36]. For the investigation of the surface area ratio, we also counted the number of black dots as the number (n) of TNTs from the uncovered TNTs FESEM images of 20 V, 30 V, 40 V, 50 V, samples (Supplementary Material). The inner surface area of a single tube would be $2r\pi L$. Therefore, the inner surface area of TNTs samples could be calculated via $2r\pi Ln$ in the images area. Then we converted the number (n) of TNTs in the images area to the number (N) of TNTs in 1 μm^2 area as the TNTs density per square micrometer. The

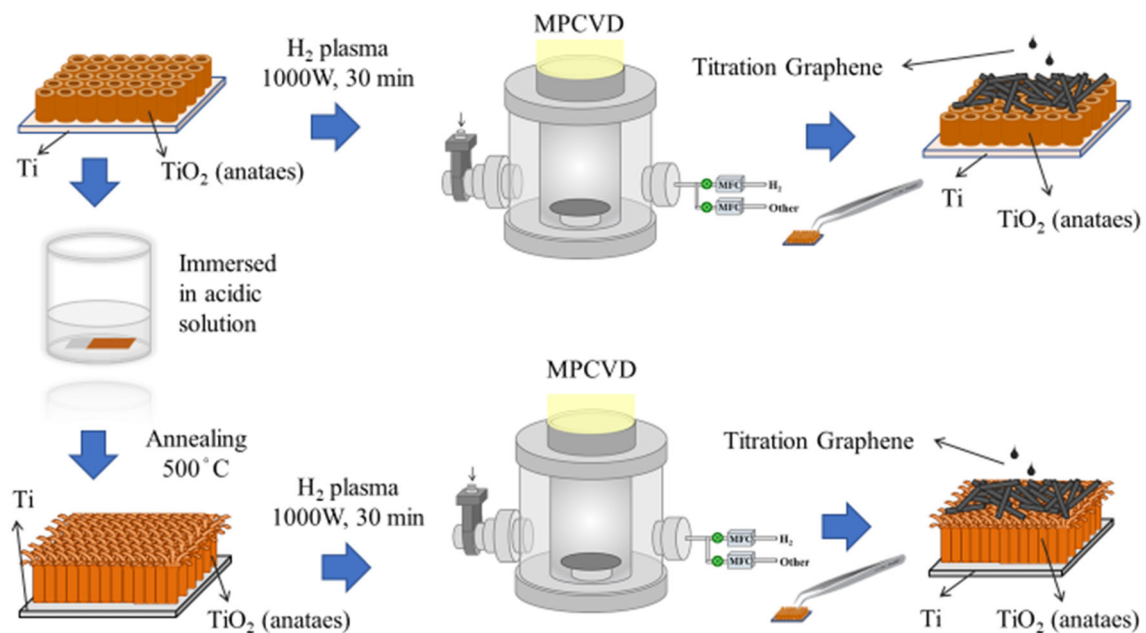


Fig. 1 Schematic diagrams of the fabrication process for Gr/TNTs and Gr/TNBs

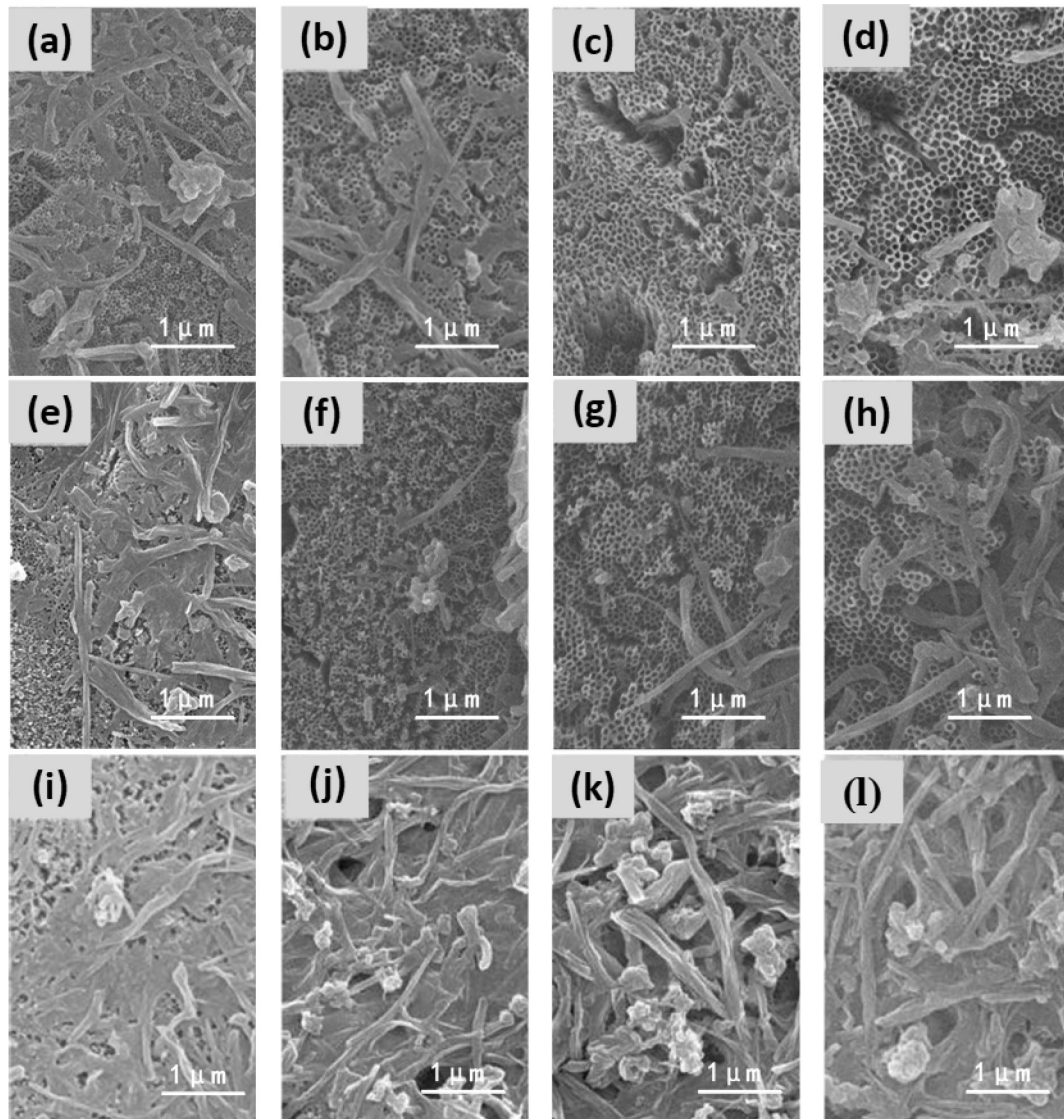


Fig. 2 FESEM images of the surface morphology of Gr/TNTs fabricated with applied voltages of **a** 20 V, **b** 30 V, **c** 40 V, **d** 50 V in 0.3 ml Gr, **e** 20 V, **f** 30 V, **g** 40 V, **h** 50 V in 0.6 ml Gr and **i** 20 V, **j** 30 V, **k** 40 V, **l** 50 V in 0.9 ml Gr

calculating results of formula of $2r\pi Ln$ could be the surface area ratio. Note that the value of plan surface area without tube punched should be a sensing area but too small compared with the tube inner surface area. Table 1 is summarized from the supplemental data and found that the surface area ratio is increased as the dimension of nanotube increased. Unfortunately, the estimating error of surface area ratio comes not only from the diameter estimation but also from the identification, counting, and the estimating length of tube. Another uncertainty is whether all the measured length of tube is the effective sensing length due to the hydrogen diffusion effect. Moreover, the image counted is a random sampling area

via FESEM image, not the whole sensing area. Therefore, this calculation only confirmed that the surface area ratio is positive dependent on the processing voltage. Figure 3 shows that TNBs without Gr covering present a rough morphology, sharp edges, bundled structures. Additionally, the bundles, edges and morphologies of the TNBs become larger, sharper and rougher as increasing electrochemical anodization applied voltages. This phenomenon may be owing to the fact that a larger aperture of nanotube can support more space for post-treatment to form a longer and larger nano-bugle.

Figure 4a shows the Raman spectra of the 0.3 ml Gr/TNBs fabricated with 20–50 V as a representative

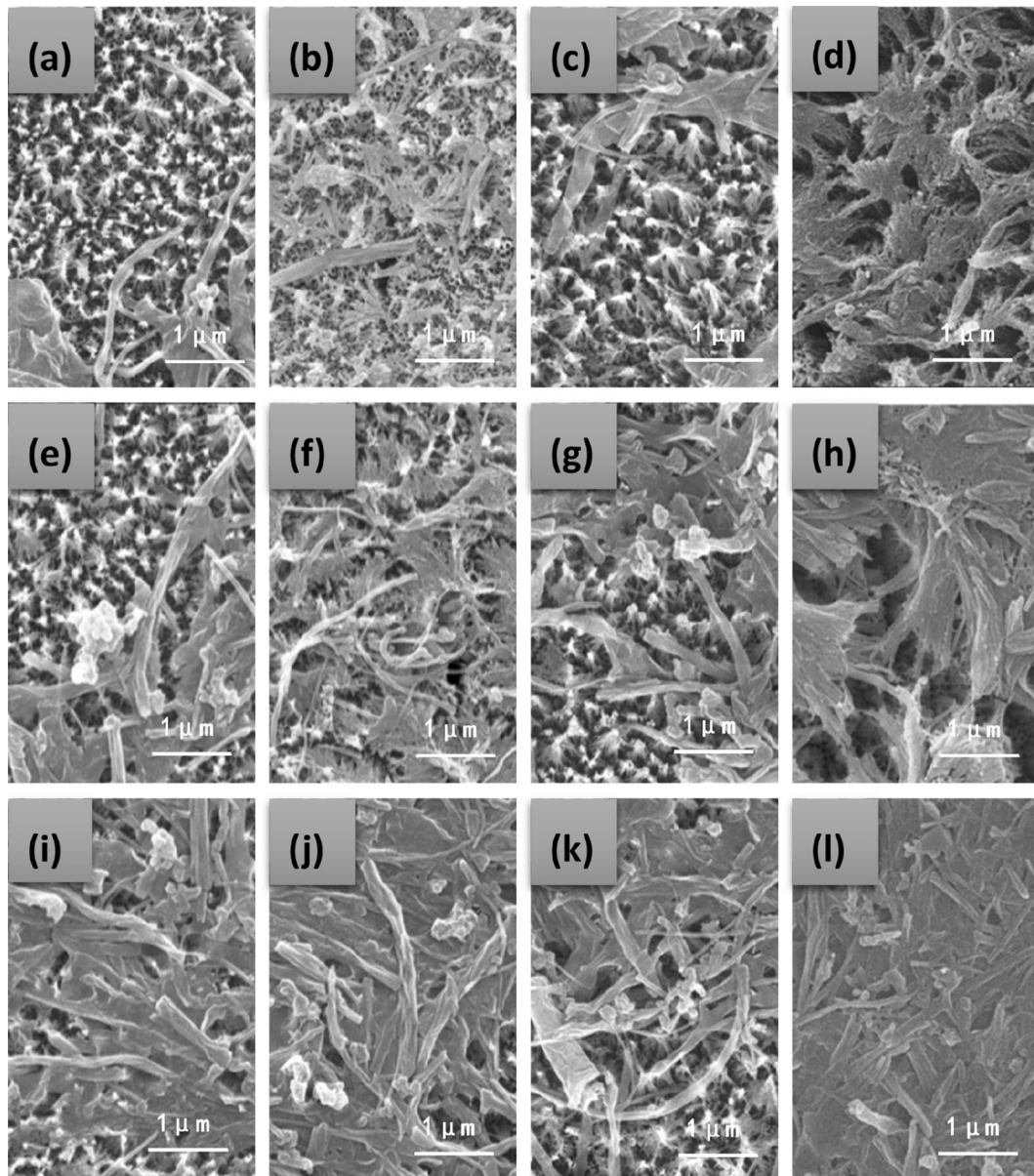


Fig. 3 FESEM images of the surface morphology of Gr/TNBs fabricated with applied voltages of **a** 20 V, **b** 30 V, **c** 40 V, **d** 50 V in 0.3 ml Gr, **e** 20 V, **f** 30 V, **g** 40 V, **h** 50 V in 0.6 ml Gr and **i** 20 V, **j** 30 V, **k** 40 V, **l** 50 V in 0.9 ml Gr

Table 1 Calculating results of surface area ratio with various fabricating voltages estimated from uncovered FESEM images

Applied voltages (V)	Diameter (nm)	Length (μm)	Counted tubes	Density ($1/\mu\text{m}^2$)	Surface area ratio (%)
20	20–30	1.4	699	424	47 ± 25
30	43–56	2.6	447	271	110 ± 15
40	71–75	3.9	259	157	140 ± 3
50	97–103	4.1	248	150	193 ± 3

observation. All curves are similar and exhibit seven peaks but different intensities. Four key features at around 144 cm^{-1} , 395 cm^{-1} , 517 cm^{-1} and 637 cm^{-1}

respectively correspond to the low-frequency O–Ti–O bending vibration [37], the anatase TiO_2 [38], and the Ti–O stretching-type vibrations [39, 40]. The other

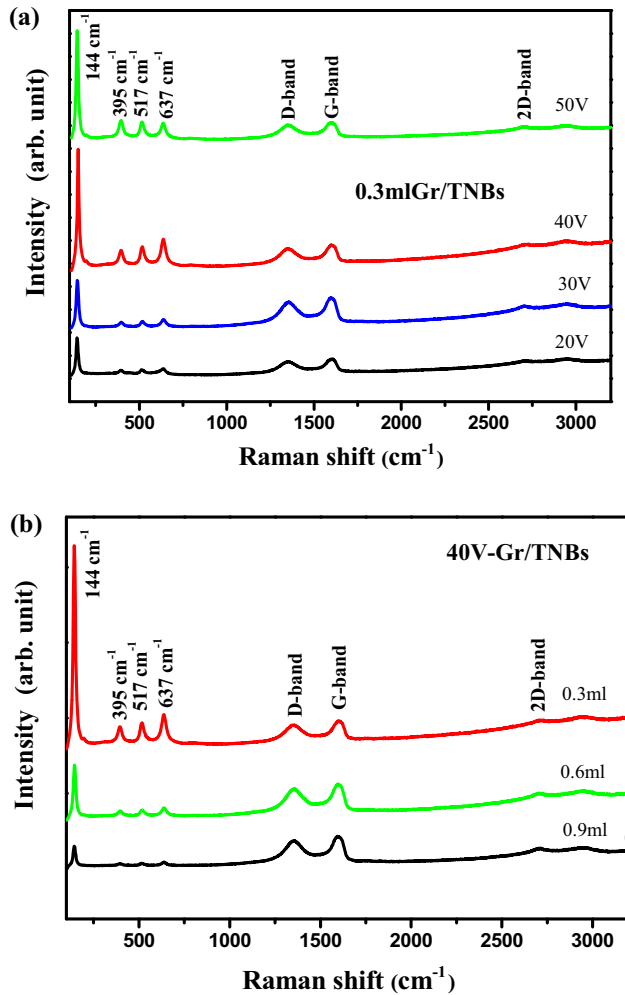


Fig. 4 Comparison of Raman spectra of the **a** 0.3 ml Gr/TNBs fabricated with 20–50 V. **b** 40 V Gr/TNBs decorated with 0.3–0.9 ml Gr compositions

three bands at 1359 cm^{-1} (ID), 1586 cm^{-1} (IG), 2705 cm^{-1} (2D) are in agreement with the characteristic peaks of Gr. Figure 4b shows the typical Raman spectra of the 40 V-Gr/TNBs decorated with different Gr compositions. Note that, the magnitude of spectra in TiO_2 would get smaller as the Gr composition increased because of the spectra intensity Gr increased. This result is in accordance with the surface morphology observation of Figs. 2 and 3, which more TiO_2 were covered with increasing Gr composition. Figure 5 shows the typical XRD patterns investigation of the Gr/TNBs with various applied voltages and confirms that all specimens still exhibit the anatase crystalline structure of TiO_2 with traditional diffraction peaks at the 25.3° (1 0 1), 37.8° (0 0 4), and 47.2° (2 0 0) planes after immersing in H_2O_2

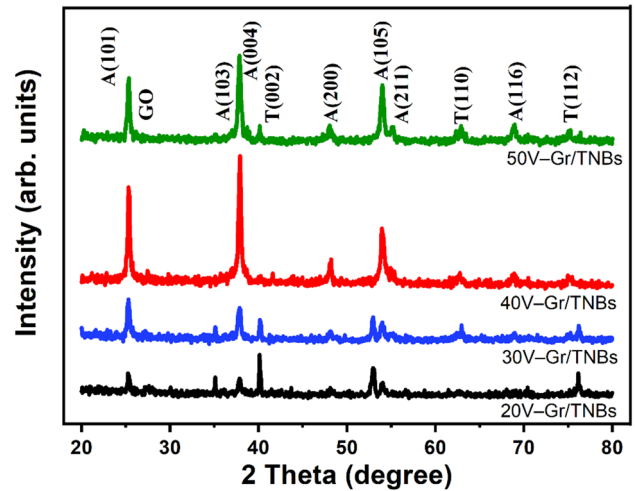


Fig. 5 X-ray diffraction patterns of Gr/TNBs fabricated with various applied voltages

solution and treating in 1000 W power plasma. Table 2 collectively list the comparisons of the full width at half maximum (FWHM) of the diffraction peak and crystallite sizes of the Gr/TNTs and Gr/TNBs corresponding to applied voltages of 20, 30, 40, and 50 V, respectively. The FWHM of the diffraction peak at the 25.3° of Gr/TNTs and Gr/TNBs fabricated with applied voltages of 20, 30, 40, and 50 V are respectively $0.38, 0.37, 0.32,$ and 0.33 cm^{-1} , and $0.37, 0.35, 0.31,$ and 0.34 cm^{-1} . The sharper characteristic diffraction peaks indicate that specimens fabricated at an applied voltage of 40 V have better crystallization. Additionally, the crystallite sizes of Gr/TNTs and Gr/TNBs fabricated with applied voltages of 20, 30, 40, and 50 V are respectively 20.3, 21.3, 25.4, and 24.7 nm, and 22.1, 23.0, 25.8, and 23.9 nm. This calculation also indicated an improvement in crystallinity while the fabrication voltages increased to 40 V.

Table 2 The full width at half maximum (FWHM) of the diffraction peak at the 25.3° and crystallite sizes of Gr/TNTs and Gr/TNBs fabricated with applied voltages of 20, 30, 40, and 50 V

Voltage	A(101) (FWHM cm^{-1}) Gr-TNTs\Gr-TNBs	Crystallite size (nm) Gr-TNTs\Gr-TNBs
20	0.383\0.366	20.525\22.064
30	0.374\0.350	21.729\23.009
40	0.321\0.313	25.624\25.778
50	0.332\0.337	24.432\23.863

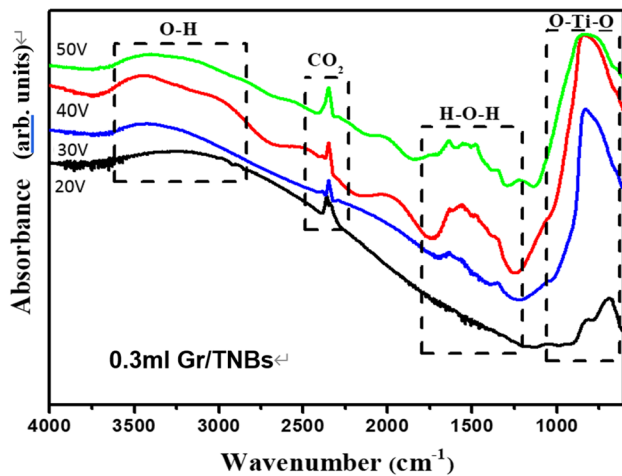


Fig. 6 Fourier transfer IR (FTIR) of the 0.3 ml Gr/TNBs corresponding to different applied voltage

Figure 6 shows the Fourier transfer IR (FTIR) covers the range of 600–4000 cm^{-1} on the 0.3 ml Gr/TNBs corresponding to different applied voltage. Four vibrational modes can be recognized at 830–930, 1620–1640, 2300–2350, and 3100–3600 cm^{-1} . The spectra peak at around 830–930 cm^{-1} presents a low-frequency O–Ti–O bending vibration. The peak at around 2300–2350 cm^{-1} is associated with the CO_2 asymmetrical stretching mode. The IR absorption spectra exhibit the absorption peaks for increasing the O–H bending vibration at 1620–1640 cm^{-1} and the OH stretching vibration at 3100–3600 cm^{-1} [41]. The absorption spectra became stronger as the applied voltages increased to 40 V, indicating an improvement of bonding strength, which is consistent to the XRD analysis results. Note that, the absorption spectra of the Gr can't be found in the FTIR spectra of Fig. 6 because the bonding strength of TiO_2 are too strong to cover the respective values of the Gr.

Figures 7a–c, and 8a–c collectively display the characteristic responses of the Gr/TNTs and Gr/TNBs sensors which were fabricated with applied voltages of 20–50 V and decorated with different Gr compositions, measured in various hydrogen gas concentration injection and pumping, respectively. All the function is performed at room temperature. The responses of the hydrogen gas sensing are defined as $[(R_{\text{hydrogen}} - R_{\text{air}})/R_{\text{air}}]$, where R_{hydrogen} is the measured resistance at each hydrogen gas concentration, and R_{air} is the measured resistance in the atmosphere. The all figures reveal that the magnitude of the sensor response reasonably decreased with

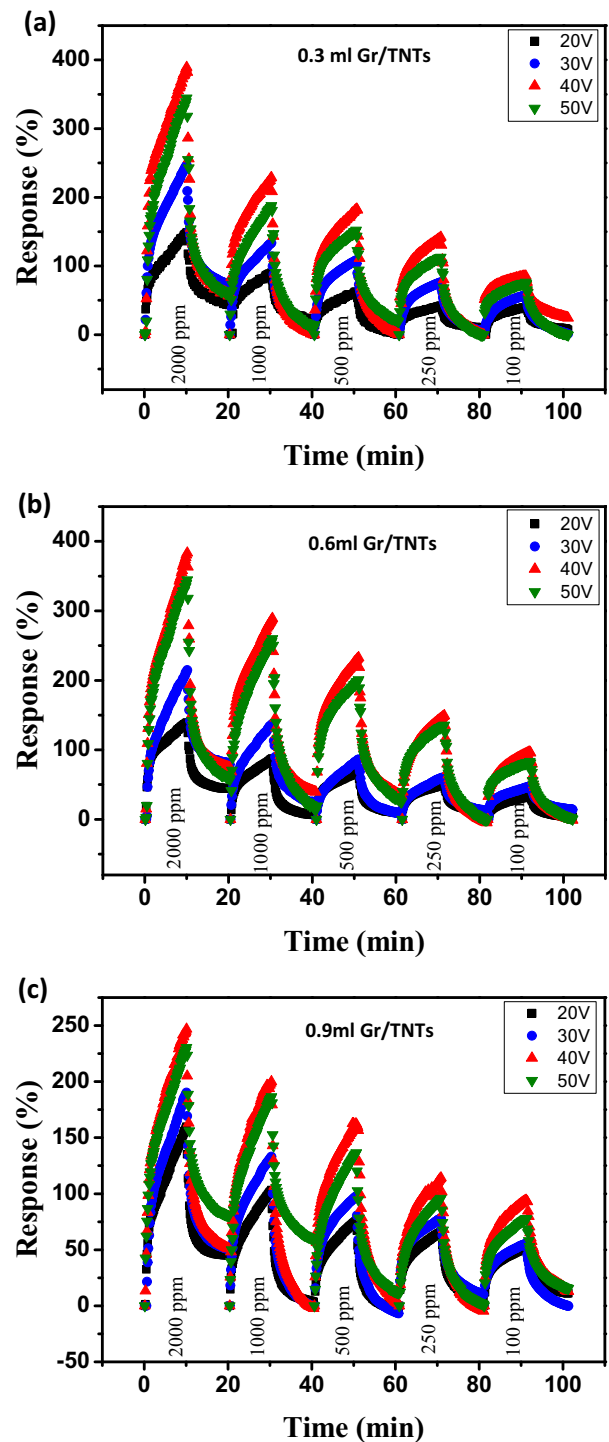


Fig. 7 Responses of a 0.3 ml, b 0.6 ml, c 0.9 ml Gr/TNTs sensors with various fabrication voltages by injection and pumping hydrogen gas concentration in 2000, 1000, 500, 250, and 100 ppm

decreasing hydrogen gas concentration. Noticeably, the responses of the 40 V fabrication specimen are considerably higher than those of the other

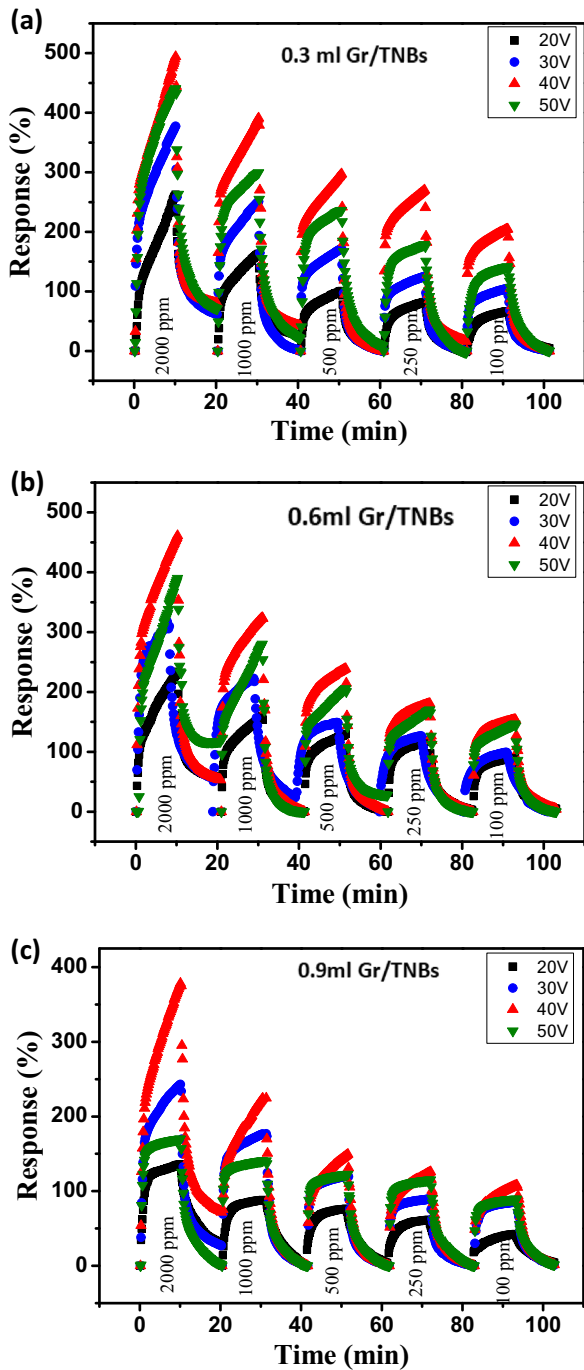


Fig. 8 Responses of **a** 0.3 ml, **b** 0.6 ml, **c** 0.9 ml Gr/TNBs sensors with various fabrication voltages by injection and pumping hydrogen gas concentration in 2000, 1000, 500, 250, and 100 ppm

specimens which may be due to the good crystal quality. Therefore, the surface area ratio is not the only dominant factor. Focusing on the specimen with

40 V fabrication, the measured responses of the 0.3 ml Gr/TNBs are around 389%, 263%, 202%, 142%, and 97% while the injected hydrogen gas concentration are 2000, 1000, 500, 250, and 100 ppm, respectively. On the other hand, the measured responses of the 0.3 ml Gr/TNBs on the same operating sequences of hydrogen atmospheres are respectively around 494%, 391%, 297%, 270%, and 205%. The bugle-shape structures sensors show higher responses than the corresponding tubular structures sensors, indicating a sensing property improvement via altering sensing surface morphologies. This observation can be attributed to the fact that the bugle-shape structure is with more effective reaction surface for the gas diffusion than the tube-shape structure. In addition, these figures also show that the magnitude of the sensing response decreased dramatically with increasing Gr composition. Therefore, Gr decorating on the sensing surface of TiO₂ can alter but not enhance the gas responsivity.

We focus the observation on the 40 V fabricated specimens for further analysis. Figure 9a and b respectively depict the sensitivity of the tubular and bugle-shape specimens with respect to the Gr composition corresponding to gas concentration. Bugle-shape specimens show the gas sensitivity regularly decreased as increasing the Gr composition. This finding seems to suggest that the bugle-shape structures can be more suitable for Gr evenly dispersing on the sensing surface than the tubular structure. In a more precise description, gas sensitivity measured on the fixed gas concentration shows a strong linear relationship between the responsivity and the Gr composition. Therefore, a composition effect is found in the bugle-shape specimens. It is worth mentioning that Gr is a 2D nanomaterial which possibly could be fitted with the surface of bugle-shape instead of covering on the top of the morphologies. This smoothly spread Gr result in a composition effect with increasing Gr components. Multilayers investigation had been reported that the response changes as the thickness of the nanolayers changes [6]. Sensing study of nanoscale film thickness had also inferred that less thickness of the film resulted in much better performance [7]. On the other hand, Hydrogen gas sensitivity of tubular structure samples did not clearly demonstrate the composition effect in the low gas concentration (100 ppm) ambience operation but show the aggravation of composition influence in the high gas concentration

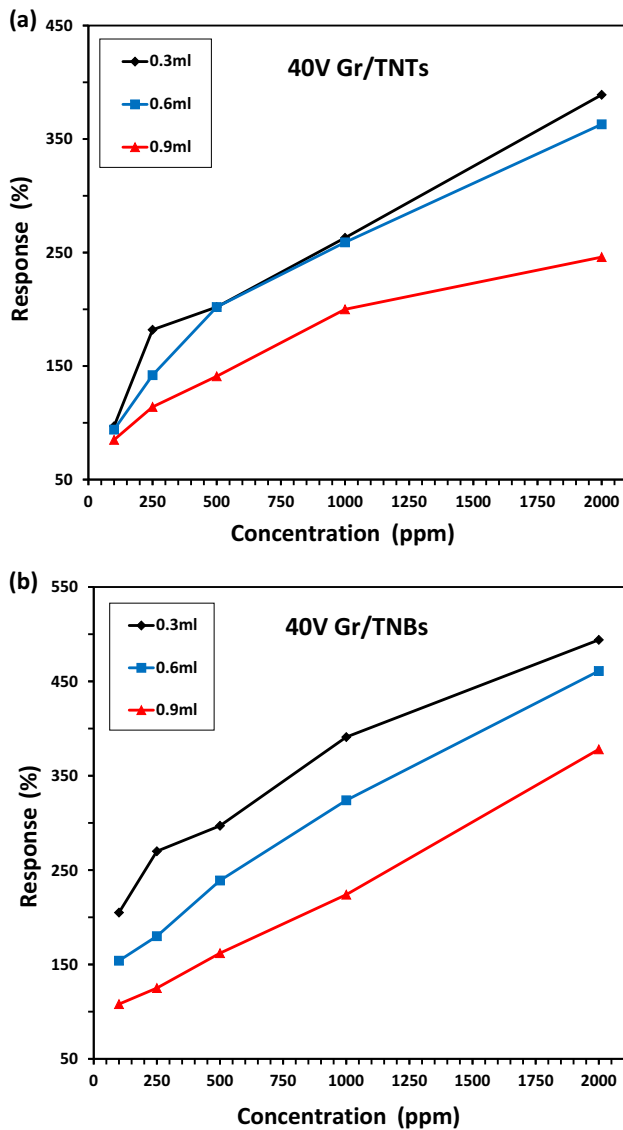


Fig. 9 Comparison of responsivity in 40 V **a** Gr/TNTs, **b** Gr/TNBs sensors decorated with various Gr compositions corresponding to hydrogen gas concentration

(2000 ppm) ambience operation. In other words, the increase of Gr composition hardly affected the responsivity in the relative low gas concentration environment. The exact interacting mechanism is still unclear and more complicated because the chemical contaminants on graphene could easily affect the absorption of gas molecules [42]. Prior field emission study has been proved that good adhesion of Gr to conductive substrates via plasma treatment can lessen the electrical resistivity on the interface layer [43]. This means that good electric conductivity on

interface supports the gas responsivity signals of Gr transmitting to TiO_2 substrates. However, good adhesion on interface also reduces the effective sensing surface area of bugle-shape structures. Accordingly, the gas sensing capability of bugle-shape sensor in this study does not increase while increasing the Gr component but decrease as more Gr adhering. On the contrary, the low gas concentration sensing degree of the tubular sensor is not affected by varying the Gr components. It may be due to the fact that the Gr is only attached on the top of the tube instead of fitting the inner wall surface of the tube. Therefore, the sensing surface area of tubular structure is not significantly reduced. This finding also suggests that Hydrogen gas can reach the tubular surface via passing through Gr. Therefore, adding layered Gr components suspended on the top of tube does not significantly vary the gas sensibility. Diagrammatic sketch of Fig. 10a–c and d–f, respectively illustrate the possible sensing mechanism of the tubular and bugle-shape specimens corresponding to the Gr composition. Figure 10a–c depict the Hydrogen gas passing through different Gr components layers suspending on the top of tubular structures and reaching the tubular surface. Figure 10d–f depict the Gr components layers attaching on the inner wall surface of the bugle-shape structures and reducing the effective sensing surface area.

The gas sensitivity of Gr/TNBs specimens show a composition effect with increasing Gr components. On the contrary, increasing Gr components does not dominate the gas sensing capability of the Gr/TNTs specimens in relatively low gas concentration environment. For the confirmation of this feature, the tubular structure samples with smaller and larger apertures respectively fabricated with applied voltage of 30 V and 50 V have also been inspected. Figure 11 depicts the responsivity of 30 V- and 50 V-Gr/TNTs sensors decorated with lighter and heavier Gr compositions corresponding to hydrogen gas concentration. The comparisons prove again that both kinds of the tubular specimens with different apertures can hardly be changed the responsivity in the relatively low gas concentration atmosphere by operating the Gr composition.

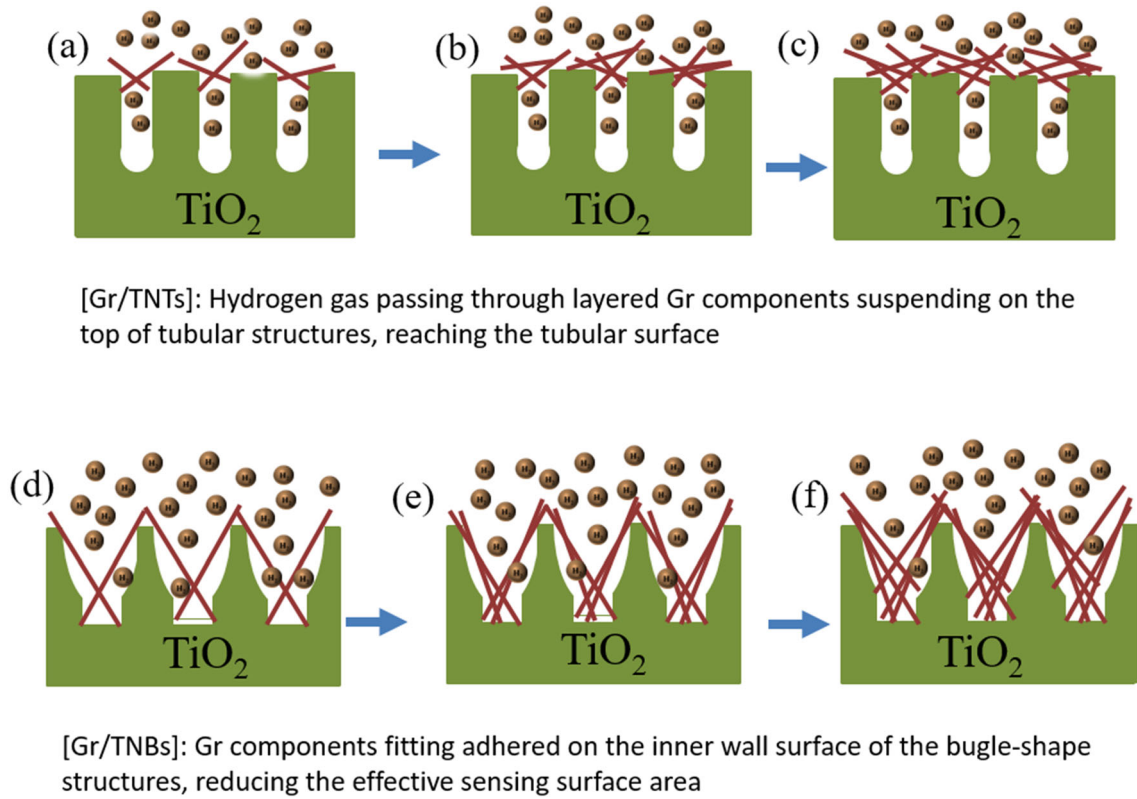


Fig. 10 Diagrammatic sketch illustration of possible sensing mechanism of the a–c tubular and d–f bugle-shape specimens corresponding to the Gr composition

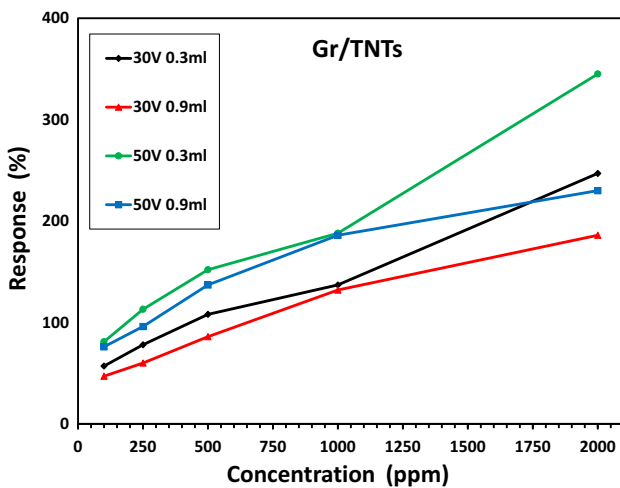


Fig. 11 Comparison of responsivity in 30 V– and 50 V– Gr/TNTs sensors decorated with lighter and heavier Gr compositions corresponding to hydrogen gas concentration

4 Conclusion

In summary, Hydrogen gas sensors with composite structures of Gr/TNTs and Gr/TNBs are successfully synthesized from the TNTs and TNBs via titration Gr

and confirmed by FESEM observation, Raman spectra comparisons, XRD and FTIR measurement. The Gr/TNBs sensors show higher responses than the corresponding Gr/TNTs sensors indicating a gas sensing improvement over 100–2000 ppm. Hydrogen gas sensitivity of 40 V Gr/TNBs measured on the fixed gas concentration shows a strong linear relationship between the responsivity and the Gr composition. A composition effect are found as Gr components increased on the bugle-shape specimens because the 2D nanomaterial possibly could be well fitted on the surface of bugle-shaped structures. In the Hydrogen gas sensitivity of 40 V-Gr/TNBs measurement, the increase of Gr component hardly affected the responsivity of tubular structure sensors in the relative low gas concentration (100 ppm) environment because the Hydrogen gas can reach the tubular surface via diffusing through the 2D nanomaterial just covered on the top of the morphologies. Gr/TNTs fabricated with 30 V and 50 V are also conformed to this observation.

Acknowledgements

This work was partly supported by the Minister of Science Technology of Taiwan under grant no. MOST-101-2622-E-011-021-CC3 and the Fuzhou Polytechnic High Level Talents Start Up Funds (FZYRCQD201903).

Author contributions

B-RH: Conceptualization; B-RH: methodology; Y-JC: Formal analysis and investigation; S-CH: writing—original draft preparation; S-CH: writing—review and editing; B-RH: resources; B-RH, S-CH: funding acquisition and supervision.

Data availability

The data that support the findings of this study are available from the corresponding author, upon reasonable request.

Code availability

Not applicable.

Declarations

Conflict of interest The authors declare no competing financial interest.

Ethical approval Not applicable.

Consent to participate Not applicable.

Consent for publication Not applicable.

Supplementary Information: The online version contains supplementary material available at <http://doi.org/10.1007/s10854-022-07786-w>.

References

- J. Xi, X. Huang, M. Hu et al., Dependence of laser parameters on structural properties of pulsed laser-deposited MoS₂ thin films applicable for field effect transistors. *J. Mater. Sci. Mater. Electron.* **31**, 21118–21127 (2020)
- A. Abderrahmane, C. Woo, P.J. Ko, Tunable optoelectronic properties of a two-dimensional graphene/ α -In₂Se₃/graphene-based ferroelectric semiconductor field-effect transistor. *J. Mater. Sci. Mater. Electron.* **32**, 20252–20258 (2021)
- M.K. Anvarifard, Z. Ramezani, I.S. Amiri et al., Profound analysis on sensing performance of Nanogap SiGe source DM-TFET biosensor. *J. Mater. Sci. Mater. Electron.* **31**, 22699–22712 (2020)
- J.L. Wang, J.H. Shang, Y.J. Guo et al., Hydrophobic metal organic framework for enhancing performance of acoustic wave formaldehyde sensor based on polyethyleneimine and bacterial cellulose nanofilms. *J. Mater. Sci. Mater. Electron.* **32**(14), 18551–18564 (2021)
- Y. Zhao, X.-G. Li, X. Zhou, Y.-N. Zhang, Review on the graphene based optical fiber chemical and biological sensors. *Sensors Actuators B* **231**, 324–340 (2016)
- O. Lupan, D. Santos-Carballal, N. Ababii, N. Magariu, S. Hansen, A. Vahl, L. Zimoch, M. Hoppe, T. Pauporté, V. Galstyan, V. Sontea, L. Chow, F. Faupel, R. Adelung, N.H. de Leeuw, E. Comini, TiO₂/Cu₂O/CuO multi-nanolayers as sensors for H₂ and volatile organic compounds: an experimental and theoretical investigation. *ACS Appl. Mater. Interfaces* **13**, 32363–32380 (2021). <https://doi.org/10.1021/acsami.1c04379>
- Z. Li, A.A. Haidry, T. Plecenik, M. Vidis, B. Grancic, T. Roch, M. Gregor, P. Durina, Z.J. Yao, A. Plecenik, Influence of nanoscale TiO₂ film thickness on gas sensing properties of capacitor-like Pt/TiO₂/Pt sensing structure. *Appl. Surf. Sci.* (2020). <https://doi.org/10.1016/j.apsusc.2019.143909>
- J. Ding, L. Cheng, Preparation of Ti³⁺ self-doped TiO_xNRs/rGO composite: application in supercapacitors. *J. Mater. Sci. Mater. Electron.* **32**, 19947–19957 (2021)
- S. Saranya, P.N. Deepa, Evolution of novel rGO/ZrHCF composite and utility in electrocatalysis towards nanomolar detection of sodium nitrite and ferulic acid. *J. Mater. Sci. Mater. Electron.* **31**, 18923–18936 (2020)
- S.M. Firdaus, A.S. Anasyida, S.A. Zubir et al., Graphene/polyaniline nanocomposites: effect of in-situ polymerization and solvent blending methods with dodecylbenzene sulfonic acid surfactant. *J. Mater. Sci. Mater. Electron.* **31**, 15805–15821 (2020)
- V.S. Leão-Neto, A.C. da Silva, L.P. Camargo et al., Fabrication of rGO/ α -Fe₂O₃ electrodes: characterization and use in photoelectrocatalysis. *J. Mater. Sci. Mater. Electron.* **31**, 16882–16897 (2020)
- E. Mainimo, G.W. Ejuh, J.M.B. Ndjaka, Effect of metalation on some graphene nanoribbons for potential application as donor in organic photovoltaic cells. *J. Mater. Sci. Mater. Electron.* **31**, 21923–21933 (2020)

13. P. Songkeaw, K. Onlaor, T. Thiwawong et al., Transparent and flexible humidity sensor based on graphene oxide thin films prepared by electrostatic spray deposition. *J. Mater. Sci. Mater. Electron.* **31**, 12206–12215 (2020)
14. L. Torrisi, L. Silipigni, G. Salvato, Graphene oxide/Cu junction as relative humidity sensor. *J. Mater. Sci. Mater. Electron.* **31**, 11001–11009 (2020)
15. C.G. Ünlü, Investigation of physical properties of Fe₂O₃ and graphene-based sandwich-type electrodes for biosensor technology. *J. Mater. Sci. Mater. Electron.* **31**, 21248–21259 (2020)
16. S. Liu, W. Zeng, Q. Guo et al., Metal oxide-based composite for non-enzymatic glucose sensors. *J. Mater. Sci. Mater. Electron.* **31**, 16111–16136 (2020)
17. M. Dong, H. Hu, S. Ding et al., High-performance non-enzymatic glucose-sensing electrode fabricated by α -nickel hydroxide-reduced graphene oxide nanocomposite on nickel foam substrate. *J. Mater. Sci. Mater. Electron.* **32**, 19327–19338 (2021)
18. S.A. Shabbir, A. Imran, M.G.B. Ashiq et al., Photoelectrochemical response of non-enzymatic glucose biosensing for graphene, carbon nanotubes and BiVO₄ nanocomposites. *J. Mater. Sci. Mater. Electron.* (2021). <https://doi.org/10.1007/s10854-021-06310-w>
19. P. Liu, M. Chen, C. Xiong et al., Flexible and highly sensitive graphene/carboxymethyl cellulose films for bending sensing. *J. Mater. Sci. Mater. Electron.* **31**, 14118–14127 (2020)
20. A. Shahzad, Z. Chen, A.A. Haidary et al., Piezoelectric pressure sensors based on GO-modified P(VDF-TrFE) fibers for vacuum applications. *J. Mater. Sci. Mater. Electron.* **31**, 18627–18639 (2020)
21. Q. Liu, Y. Zhang, A. Li et al., Reduced graphene oxide-coated carbonized cotton fabric wearable strain sensors with ultralow detection limit. *J. Mater. Sci. Mater. Electron.* **31**, 17233–17248 (2020)
22. Y. Zhang, H. Tang, A. Li et al., Extremely stretchable strain sensors with ultra-high sensitivity based on carbon nanotubes and graphene for human motion detection. *J. Mater. Sci. Mater. Electron.* **31**, 12608–12619 (2020)
23. K. Chetankumar, B.E.K. Swamy, T.S.S.K. Naik, A reliable electrochemical sensor for detection of catechol and hydroquinone at MgO/GO modified carbon paste electrode. *J. Mater. Sci. Mater. Electron.* **31**, 19728–19740 (2020)
24. R.N. Suhanto, S. Harimurti, N.L.W. Septiani et al., Sonochemical synthesis of magnetic Fe₃O₄/graphene nanocomposites for label-free electrochemical biosensors. *J. Mater. Sci. Mater. Electron.* **31**, 15381–15393 (2020)
25. R. Ramadan, S.K. Abdel-Aal, Facile synthesis of nanostructured ZnO-rGO based graphene and its application in wastewater treatment. *J. Mater. Sci. Mater. Electron.* (2021). <https://doi.org/10.21203/rs.3.rs-260195/v1>
26. J. Gao, Y. Wang, Y. Han et al., Graphene-based field-effect transistors integrated with microfluidic chip for real-time pH monitoring of seawater. *J. Mater. Sci. Mater. Electron.* **31**, 15372–15380 (2020)
27. D. Wibowo, Y. Sufandy, I. Irwan et al., Investigation of nickel slag waste as a modifier on graphene-TiO₂ microstructure for sensing phenolic compound. *J. Mater. Sci. Mater. Electron.* **31**, 14375–14383 (2020)
28. J. Sun, P. Song, D. Liang et al., Enhanced trimethylamine sensing properties of ternary rGO/MoO₃/Au hybrid nanomaterials. *J. Mater. Sci. Mater. Electron.* **31**, 20549–20560 (2020)
29. T.O. Wehling, K.S. Novoselov, S.V. Morozov, E.E. Vdovin, M.I. Katsnelson, A.K. Geim, A.I. Lichtenstein, Molecular doping of graphene. *Nano Lett.* **8**, 173–177 (2008)
30. O. Leenaerts, B. Partoens, F.M. Peeters, Adsorption of H₂O, NH₃, CO, NO₂, and NO on graphene: a first-principles study. *Phys. Rev. B Condens. Matter Mater. Phys.* **77**, 125416 (2008)
31. F. Schedin, A.K.K. Geim, S.V.V. Morozov, E.W. Hill, P. Blake, M.I.I. Katsnelson, K.S.S. Novoselov, Detection of individual gas molecules adsorbed on graphene. *Nat. Mater.* **6**, 652–655 (2007)
32. L. Zhong et al., Low-cost fabrication of highly sensitive room temperature hydrogen sensor based on ordered mesoporous Co-doped TiO₂ structure. *App. Phys. Lett.* **111**(3), 032104 (2017)
33. B. Lyson-Sypien et al., Nanopowders of chromium doped TiO₂ for gas sensors. *Sensors Actuators B Chem.* **175**, 163–172 (2012)
34. Ş Erdem, A. Onur, Z.Ö. Zafer, The effect of Pd on the H₂ and VOC sensing properties of TiO₂ nanorods. *Sensors Actuators B Chem.* **229**, 692–700 (2016)
35. A.A. Haidry, E.-S. Andrea, S. Bilge, Effect of Pt/TiO₂ interface on room temperature hydrogen sensing performance of memristor type Pt/TiO₂/Pt structure. *Sensors Actuators B Chem.* **253**, 1043–1054 (2017)
36. B.-R. Huang, J.-C. Lin, T.-C. Lin, Y.-J. Chen, Aggregated TiO₂ nanotubes with high field emission properties. *Appl. Surf. Sci.* **311**, 339–343 (2014)
37. H. Tang et al., Electrical and optical properties of TiO₂ anatase thin films. *J. Appl. Phys.* **75**(4), 2042–2047 (1994)
38. P.P. Lottici et al., Raman scattering characterization of gel-derived titania glass. *J. Mater. Sci.* **28**(1), 177–183 (1993)
39. J. Liang, G. Zhang, TiO₂ nanotip arrays: anodic fabrication and field-emission properties. *ACS Appl. Mater. Interfaces.* **4**(11), 6053–6061 (2012)

40. R.P. Antony et al., Enhanced field emission properties of electrochemically synthesized self-aligned nitrogen-doped TiO₂ nanotube array thin films. *J. Phys. Chem. C* **116**(31), 16740–16746 (2012)
41. D.A. Panayotov, J.T. Yates Jr., *Chem. Phys. Lett.* **410**, 11 (2005)
42. Y.P. Dan, Y. Lu, N.J. Kybert, Z.T. Luo, A.T.C. Johnson, *Nano Lett.* **9**, 1472–1475 (2009)
43. S.-C. Hung, Y.-J. Chen, Enhanced field emission properties of tilted graphene nanoribbons on aggregated TiO₂ nanotube arrays. *Mater. Res. Bull.* **79**, 115–120 (2016)

Publisher's Note Springer Nature remains neutral with regard to jurisdictional claims in published maps and institutional affiliations.